

Simulated Annealing for Land Cover Classification in PolSAR Images

Georgia Koukiou

Electronics Laboratory (ELLAB), Physics Department, University of Patras, Patras, Greece

Email: gkoukiou@upatras.gr

How to cite this paper: Koukiou, G. (2022) Simulated Annealing for Land Cover Classification in PolSAR Images. *Advances in Remote Sensing*, 11, 49-61. <https://doi.org/10.4236/ars.2022.112004>

Received: March 31, 2022

Accepted: June 11, 2022

Published: June 14, 2022

Copyright © 2022 by author(s) and Scientific Research Publishing Inc. This work is licensed under the Creative Commons Attribution International License (CC BY 4.0). <http://creativecommons.org/licenses/by/4.0/>



Open Access

Abstract

Simulated Annealing (SA) is used in this work as a global optimization technique applied in discrete search spaces in order to change the characterization of pixels in a Polarimetric Synthetic Aperture Radar (PolSAR) image which have been classified with different label than the surrounding land cover type. Accordingly, Land Cover type classification is achieved with high reliability. For this purpose, an energy function is employed which is minimized by means of SA when the false classified pixels are correctly labeled. All PolSAR pixels are initially classified using 9 specifically selected types of land cover by means of Google Earth maps. Each Land Cover Type is represented by a histogram of the 8 Cameron's elemental scatterers by means of coherent target decomposition (CTD). Each PolSAR pixel is categorized according to the local histogram of the elemental scatterers. SA is applied in the discrete space of nine land cover types. Classification results prove that the Simulated Annealing approach used is very successful for correctly separating regions with different Land Cover Types.

Keywords

Land Cover Classification, Simulated Annealing, Fully Polarimetric SAR, Coherent Decomposition, Elemental Scatterers

1. Introduction

Land use and land cover changes constitute a challenging goal in Land cover classification procedures [1] [2]. Various types of satellite sensors provide information for Earth land cover based on all electromagnetic spectrum bands for which the atmosphere is transparent. Fifty research papers on land cover classification using satellite images are surveyed in [3]. The research papers are categorized based on different classification techniques, such as Fuzzy, Support

Vector Machine (SVM), Neural Network (NN), Bayesian models and Decision Trees. In [4] six machine-learning algorithms for land cover and land use were examined. The review in [5] shows that Sentinel-2 has a positive impact on land cover/use monitoring, specifically in monitoring of crop, forests, urban areas, and water resources. The aim of [6] is to provide the state of the art in the use of Earth Observation technology in land cover classification. The work in [7] deals with the traditional change detection techniques. In [8], the multispectral imagery of 10 m spatial resolution of a densely populated urban area, obtained from sentinel-2, is classified using Support Vector Machines, Artificial Neural Networks and Maximum Likelihood Classifiers.

Earth observation has to gain a lot from the fully polarimetric views that SAR imaging provides. In [9] a thorough analysis of polarimetry is given and the most significant target decomposition approaches are described. Inherent scatterer polarimetric properties have been exploited in SAR imagery to facilitate the detection of man-made objects in [10]. Automatic classification of the dominant scattering mechanisms associated with the pixels of polarimetric SAR images is carried out in [11]. In [12] for each pixel of the considered scene, the polarimetric covariance matrix, the coherence matrix, and the Muller matrix are exploited. Coherent Target Decomposition (CTD) methods for ship detection were proposed in [13] [14] [15] where systematic approaches for ship detection by means of the Cameron CTD [16] were presented describing the dominant scattering mechanisms of sea and ships. In [17] the co-diagonalization of the Sinclair backscattering matrix is revisited to overcome the Huynen decomposition issues. Consequently, scatterer polarimetric properties are correctly extracted leading to the proper selection of the predominant scattering mechanism. In [18] a twofold approach is presented by employing Cameron's CTD for automatic ship scatterers characterization and simultaneously mutual statistics of the scatterers are incorporated by means of the Markov property [19] [20] for correctly assessing the alternation among the elementary scatterers for ship detection. Finally, PolSAR data have been used in [21] for land cover classification by means of Markov chains representing the alternation of elementary scatterers.

Simulated annealing is a probabilistic technique for approximating the global optimum of a given function. It is often used when the search space is discrete. In land cover classification tasks, it is useful when discrete type scatterers are employed to represent the electromagnetic behavior of each SAR pixel. Accordingly, in [22] simulated annealing is applied to unsupervised SAR classification problems. A classification algorithm for multi-temporal SAR images and InSAR coherence images is developed in [23]. The research in [24] is designed to develop algorithms to apply the simulated annealing to unsupervised classification and compare the classification results with that of the K-means. In [25] two polarimetric segmentation techniques for polarimetric SAR images are compared. The proposed process in [26] helps to detect oil spills using SAR images and estimate the amount of oil spilled in a region. A sample image is evaluated using

three different meta-heuristic search algorithms including Simulated Annealing. A calculation method of simulated annealing (SA) is proposed in [27] for probability integral parameters based on single line of sight D-InSAR. A new method [28] employing Simulated Annealing in polarimetric SAR data decomposition extracts additional polarimetric information from the Synthetic Aperture Radar (SAR) images compared to other existing decomposition methods. In [29] a new optimization-based reallocation model using Simulated Annealing has been developed to realize block reallocation by evaluating the requests of landowners. Finally, significant contribution regarding Land Cover type classification has been made in [30] [31] [32] [33] and [34] regarding the formation of natural river networks under changing climate, using their spectral properties.

In the present work, the Cameron CTD is employed to characterize land cover types with the histogram of 8 different elemental scatterers. Each separate pixel of the fully polarimetric SAR image is represented by one of the elementary scatterers. The novelty of the proposed land classification approach lies on the use of Simulated Annealing global optimization method to clear up isolated scattering mechanisms in the location found in case these pixels are false classified and replace them with the behavior of their eight-connected neighbors. Nine different types of land cover are used for testing the proposed method. The achieved classification performance is significantly high. The proposed methodology is depicted in the block diagram of **Figure 1**.

The SNAP open source architecture for ESA Toolboxes [35] is used for geo-coding and rectification using ground control points. The geocoded SAR images are employed to create the scattering mechanisms map so that full correspondence with the Google Earth maps exists.

The paper is organized as follows. In section 2 the use of elemental scatterers for characterizing each pixel is explained. In section 3 the creation of the feature

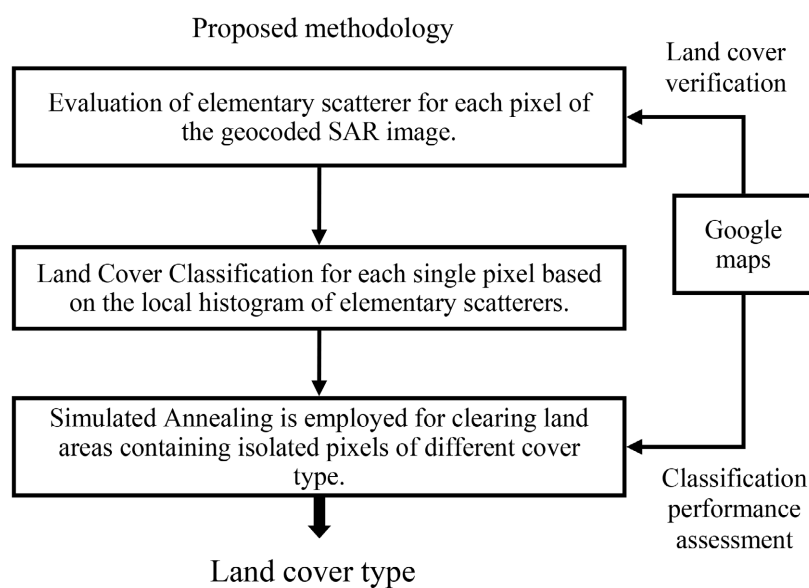


Figure 1. The proposed methodology with its three main stages.

for land cover classification by means of local histograms of elemental scatterers is discussed. In section 4 is analyzed the way the Simulated Annealing global optimization technique is applied to successfully categorize SAR pixels in various land cover types. The conclusions are drawn in section 5.

2. Elemental Scattering Features

Essential scattering features that can be used to represent the SAR pixel behaviour are those coming from the analysis of the scattering matrix of the pixel. Scattering matrix decomposition [9] [14] [16] [36] is a robust mathematical procedure to extract information from PolSAR pixels. Cameron decomposition [16] is giving emphasis to elementary scattering mechanisms with physical meaning. Reciprocity and symmetry are the two basic properties of the scatterers that can be exploited with Cameron coherent decomposition. For all monostatic SAR systems, the non-diagonal elements of the relevant backscattering matrix \mathcal{S} of a scatterer are pair wise equal. This corresponds to the reciprocity property. Furthermore, the property of symmetry is attributed to a reciprocal scatterer if it presents an axis of symmetry in the plane perpendicular to the radar line of sight (LOS). Based on Cameron's target decomposition eight elementary scatterers can be distinguished based on the properties of reciprocity and symmetry namely the trihedral, the dihedral, the dipole, the cylinder, the 1/4 wave devices and the narrow diplane. Additionally, two non-symmetric scattering mechanisms the left and the right helix are considered as elementary scattering mechanisms. As exposed analytically in [21] Cameron decomposition transforms the backscattering matrix \mathcal{S} to the backscattering vector $\vec{\mathcal{S}}$:

$$\vec{\mathcal{S}} = g \left\{ \cos \tau_{\text{sym}} \vec{\mathcal{S}}_{\text{sym}}^{\text{max}} + \sin \tau_{\text{sym}} \vec{\mathcal{S}}_{\text{sym}}^{\text{min}} \right\} \quad (1)$$

The degree of symmetry of the scatterer expresses the degree to which $\vec{\mathcal{S}}$ deviates from $\vec{\mathcal{S}}_{\text{sym}}^{\text{max}}$. In (1) if $\tau_{\text{sym}} = 0^\circ$ then the $\vec{\mathcal{S}}_{\text{sym}}^{\text{max}}$ corresponds to a fully symmetric scatterer and if the angle reaches its maximum of 45° then it corresponds to a fully asymmetric scatterer. The maximum symmetric component $\vec{\mathcal{S}}_{\text{sym}}^{\text{max}}$ can be transformed into a normalized complex vector $\hat{\mathbf{A}}(z)$ with z being referred to as the complex parameter that eventually determines the scattering mechanism. The normalized complex vector $\hat{\mathbf{A}}(z)$ is given by

$$\hat{\mathbf{A}}(z) = \frac{1}{\sqrt{1+|z|^2}} \begin{bmatrix} 1 \\ 0 \\ 0 \\ z \end{bmatrix} \quad (2)$$

Values of z corresponding to elementary scattering mechanisms are given in **Table 1**. In order to determine the scattering mechanism, we are based on the distance [21] of the complex parameter z of the scatterer under study and the reference complex parameters z_{ref} as they appear in **Table 1**:

$$d(z, z_{\text{ref}}) = \sin^{-1} \left(\min \left[d_-(z, z_{\text{ref}}), d_*(z, z_{\text{ref}}) \right] \right) \quad (3)$$

where

$$d_-(z, z_{\text{ref}}) = \sqrt{\frac{|z - z_{\text{ref}}|^2}{(1 + |z|)^2 (1 + |z_{\text{ref}}|)^2}} \tag{4}$$

and

$$d_*(z, z_{\text{ref}}) = \sqrt{\frac{|z - z_{\text{ref}}^*|^2 + (1 - |z|^2)(1 - |z_{\text{ref}}^*|^2)}{(1 + |z|)^2 (1 + |z_{\text{ref}}|)^2}} \tag{5}$$









In **Table 2** a specific color palette (MATLAB JET color map) is shown and is used for demonstration purposes for mapping the elementary scatterers revealed by the above described Cameron decomposition procedure. The employed fully polarimetric SAR data containing a part of the Vancouver region are depicted in **Figure 2**.

The high-resolution fully polarimetric SAR imagery (C-band, 5.6 cm) is coming from RADARSAT-2 platform with primary mission the all-weather maritime and

Table 1. Complex parameter z corresponding to elementary scattering mechanisms. (Obtained from [21] with the permission of the Authors).

| Complex Parameter z | Normalized Complex Vector $\hat{\mathbf{A}}(z)$ | Scattering Mechanism |
|-----------------------|---|----------------------|
| 1 | $\hat{\mathbf{A}}(1)$ | Trihedral |
| -1 | $\hat{\mathbf{A}}(-1)$ | Diplane |
| 0 | $\hat{\mathbf{A}}(0)$ | Dipole |
| +1/2 | $\hat{\mathbf{A}}(+1/2)$ | Cylinder |
| -1/2 | $\hat{\mathbf{A}}(-1/2)$ | Narrow Diplane |
| $\pm j$ | $\hat{\mathbf{A}}(\pm j)$ | 1/4 wave device |

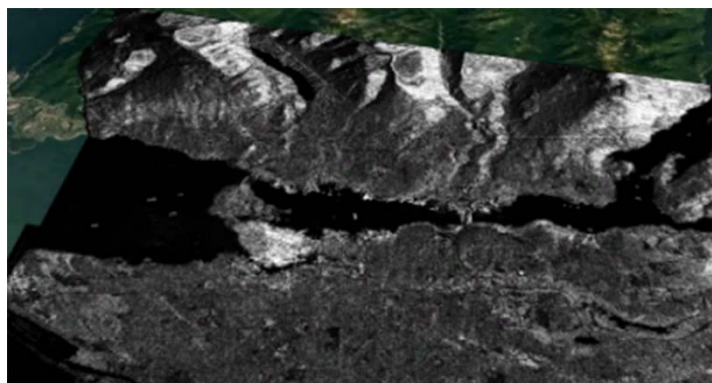
Table 2. Cameron eight Elemental Scatterers color-coding. JET color map is from MATLAB color processing. (Obtained from [21] with the permission of the Authors).

| Symmetric Elementary Scatterer | Class | Cameron Color Representation |
|--------------------------------|-------|---|
| Trihedral | 1 |  |
| Diplane | 2 |  |
| Dipole | 3 |  |
| Cylinder | 4 |  |
| Narrow Diplane | 5 |  |
| 1/4 Wave Device | 6 |  |
| Left Helix | 7 |  |
| Right Helix | 8 |  |

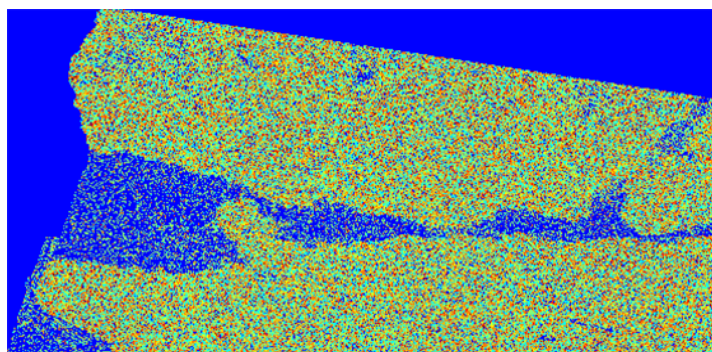
land observation. The used fully polarimetric SAR imagery is of the Wide Fine Quad-Pol, Single Look Complex, in SLC products [37]. Each pixel of the four polarimetric returns is of complex value having its I and Q components in 16-bit representation. The nominal resolution is 13.6×7.6 meters with nominal scene size 50×25 Km and incidence angle range 18 to 42 degrees. Geo-referenced data can be easily corresponded into Google Earth maps as shown in **Figure 2(a)** (Google Earth and HV SAR images co-registered by means of SNAP platform) for creating the truth maps for training and testing purposes in the land cover classification procedure to be followed. In **Figure 2(b)** each pixel of the SAR image of **Figure 2(a)** is represented by a colour from **Table 2** giving thus a sense of the elementary scatterer in each SAR cell.

3. Land Cover Type Classification

In this work the proposed feature vector for polarimetric SAR land cover classification is a simple vector of eight elements representing the elemental scatterers as they are given in **Table 2**. The land cover classification procedure is based on two distinct stages. Firstly, the normalized histogram of the eight elemental scatterers of **Table 2**, is evaluated using the regions shown in blocks in **Figure 3** which correspond to 9 different land cover types. In this way we can record the



(a)



(b)

Figure 2. (a) Google Earth and HV SAR images co-registered by means of SNAP platform. (b) Each pixel of the SAR image in (a) is represented by a color from **Table 2** giving thus a sense of the elementary scatterer in each SAR cell.

scattering behaviour of the specific land cover types by creating 9 histograms as reference prototypes for comparison. Indicative elemental scatterers' histograms of the dense residential region and the industrial regions (blocks 5 and 9 respectively in **Figure 3**) are depicted in **Figure 4**.

In the second stage, in each position (pixel) of **Figure 2**, the local normalized scatterers histogram is evaluated using a window of size 7×7 around the specific pixel. This histogram is compared with the 9 normalized reference histograms created in first stage by means of the 9 land cover types shown in **Figure 3**. The

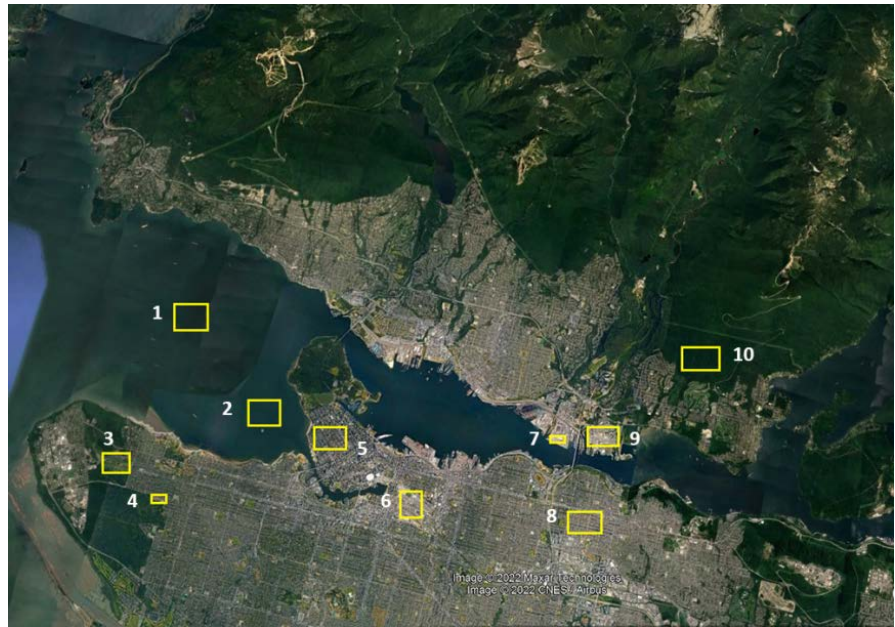


Figure 3. The ten regions with distinct Land Cover types. 1. Water A, 2. Water B, 3. Low vegetation, 4. Clear land, 5. Dense residential area, 6 and 7. Industrial fields, 8. Normal residential area, 9. Industrial Buildings, 10. Forest.

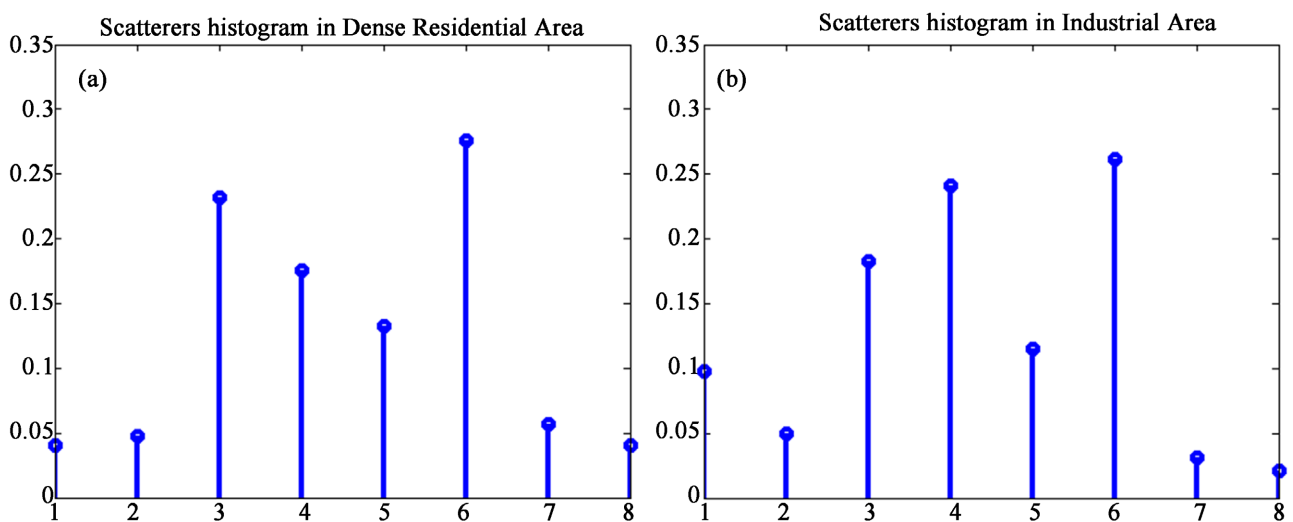


Figure 4. Normalized histograms of the eight elemental scatterers as they are given in **Table 2**. These histograms are used as reference prototypes for classifying all PolSAR pixels of **Figure 2**. (a) Scatterers histogram of the dense residential area included in block 5 of **Figure 3**. (b) Scatterers histogram of the industrial area included in block 9 of **Figure 3**.

central pixel of the 7×7 window is assigned to the land cover type for which the reference histogram is closer. Histogram closeness is found using the simple Euclidean distance of the local histogram and each one of the 9 reference histograms.

After classifying each of the PolSAR pixels by means of the above procedure the Simulated Annealing optimization method is applied in order to correct classification errors. These errors correspond to pixels labelled to belong to a specific land cover type but the surrounding 8-connected neighbours belong to a different land cover type.

Elaborating on the prototype reference histograms as those presented in **Figure 4**, the following conclusions can be drawn regarding the dominating scatterers in each type of Land Cover:

- Dense Residential area. The dominant scatterer is the 6th with the 3rd, 4th and 5th quite strong.
- Industrial area. The dominant scatterers are the 6th and the 4th with the 3rd quite strong.
- Industrial Buildings. The dominant scatterers are the 6th and the 4th with the 3rd quite strong.
- Normal Residential Area. The dominant scatterers are the 6th and the 4th with the 3rd quite strong.
- Clear Land. The dominant scatterer is the 4th with the 1st quite strong.
- Grass area and Low Vegetation. The dominant scatterers are the 6th and the 4th with the 3rd quite strong.
- Trees area (Forest). The dominant scatterer is the 6th with the 4th and the 3rd quite strong.
- Water 1 and Water 2. The dominant scatterer is the 4th with the 1st quite strong.

4. Simulated Annealing and Classification Performance

According to the land cover classification procedure described in the previous section, the pixels of the whole image in **Figure 2** are classified by assigning to each one a label of a specific land cover. The labels $l = 1, \dots, 9$, correspond to integer values and represent land cover types as they are distinguished in **Figure 3**. Since the classification is carried out according to the Euclidean distance between the reference prototype histograms and local histogram derived from the information inside the window 7×7 pixels, some areas in the final land cover mapping appear somewhat spotted, with single pixels of a category embedded in larger areas of another class. Generally, one expects the neighboring pixels to belong to the same category unless there is a real border between the areas. In order to clear spotted regions from pixels that are irrelevant to the surrounding land cover type an energy function $f(U)$ is established and its minimization is sought. This minimization is achieved by means of the Simulated Annealing global optimization technique and the energy U is decreased when a SAR pixel

categorized in a different land cover type than its eight-connected neighbors (which are of the same land cover type) it is changed to the land cover type of its neighbors.

The concept of Simulated Annealing is based on an analogy between the thermodynamic behavior of solids and large combinatorial optimization. The basic procedure involves a cooling procedure, in which a “temperature” parameter starts out high and is gradually lowered until the system is “frozen” (in a state of minimal energy U). In the simulated annealing algorithm, not only are state changes which decrease energy are accepted, but also are accepted some state changes which increase energy with a defined probability. However, the lower the temperature, the less likely is any significant energy increase. The Simulated Annealing algorithm is implemented as follows:

- 1) Choose initial temperature T_0 and assign the class label (1 to 9) to every pixel.
- 2) For each isolated pixel, change its label to the class of its eight-connected neighbors.
- 3) Compute dU and accept the change when $dU = 0$ or with a probability $\exp(-dU/T)$, when $dU > 0$.
- 4) Set $T_{\text{new}} = u * T_{\text{old}}$ ($0 < u < 1$).
- 5) Continue until $T_{\text{new}} = T_{\text{end}}$ where T_{end} is the freezing temperature.

The SA was applied simultaneously for all cover types and overall area of the image in **Figure 2**. The classification results regarding two of the land cover types are shown in **Figure 5** and **Figure 6**. In **Figure 5** are shown the classified regions belonging to Industrial Buildings land cover, while in **Figure 6** the classified regions of clear land are depicted. Similar results have been obtained for all cover types.

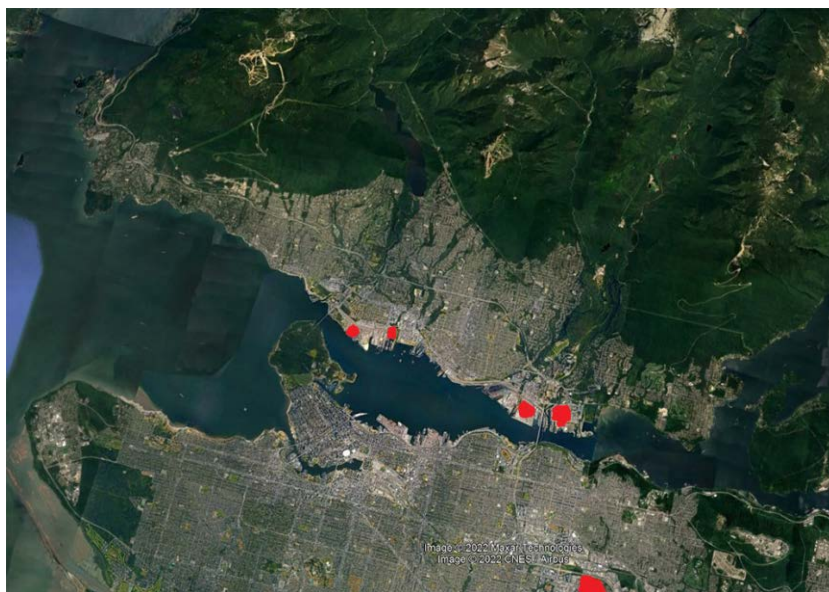


Figure 5. Industrial buildings as they are isolated when running the Simulated Annealing global optimization approach.

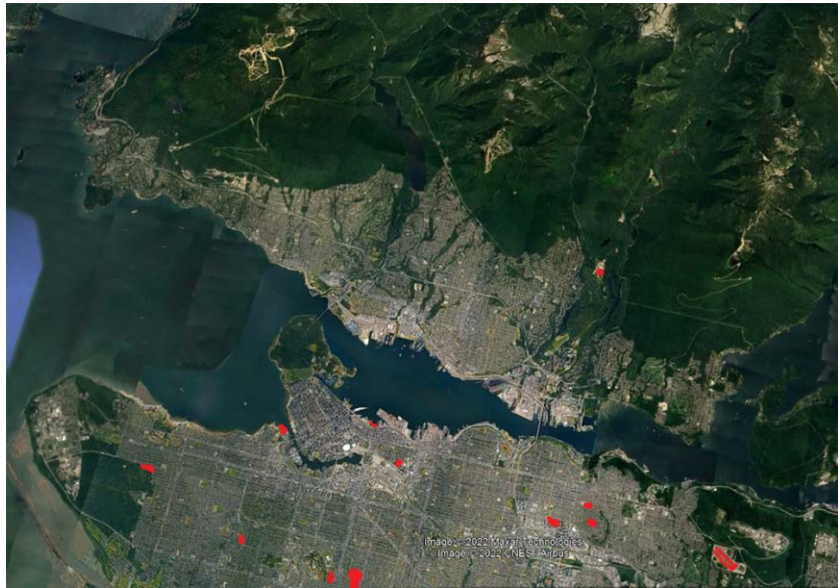


Figure 6. Regions characterized as being clear land, as they are isolated when running the Simulated Annealing global optimization approach.

Table 3. Land cover classification success by mean of Simulated Annealing.

| Land Cover Type | Classification success % |
|-------------------------|--------------------------|
| Water A | 100 |
| Water B | 100 |
| Low vegetation | 98 |
| Clear Land | 99 |
| Dense residential area | 97 |
| Industrial fields | 97 |
| Normal residential area | 99 |
| Industrial buildings | 97 |
| Forest | 100 |

The classification results obtained using the SA optimization approach are presented in **Table 3**. From the table it is obvious that the classification success is high and the application of SA radically concentrates the same pixels to the correct land cover types.

5. Conclusions

Experimentally, land cover classification is carried out using 9 specific land cover types along with the eight elemental scatterers obtained from Camerons' CTD. Firstly, the PolSAR pixels are classified based on the comparison of the histograms of the elemental scatterers in the 9 specific land cover types and the local histogram of the elemental scatterers at the position of each pixel. This first stage gives a successful land cover classification which however leads to many

pixels being categorized in a different land cover type than the surrounding pixels. To avoid this incompatibility the Simulated Annealing is used in this work as a global optimization technique applied in the discrete search space of the land cover types in order to change the characterization of these pixels to match the surrounding land cover type. An energy function was employed which is minimized by means of the Simulated Annealing method when the false classified pixels are correctly labeled. For the Vancouver region in which the whole procedure was applied a totally successful classification performance was achieved.

Comparisons with already existing techniques with the method proposed in this paper reveal that the method proposed here is unique in the sense that SA is for first time applied in the discrete space of $N = 9$ Land Cover Types in order to reorganize false labeled PolSAR pixels.

Conflicts of Interest

The author declares no conflicts of interest regarding the publication of this paper.

References

- [1] Tong, X.Y., Xia, G.S., Lu, Q., Shen, H., Li, S., You, S. and Zhang, L. (2020) Land-Cover Classification with High-Resolution Remote Sensing Images Using Transferable Deep Models. *Remote Sensing of Environment*, **237**, Article ID: 111322. <https://doi.org/10.1016/j.rse.2019.111322>
- [2] Tsagaris, V., Anastassopoulos, V. and Lampropoulos, G.A. (2005) Fusion of Hyperspectral Data Using Segmented PCT for Color Representation and Classification. *IEEE Transactions on Geoscience and Remote Sensing*, **43**, 2365-2375. <https://doi.org/10.1109/TGRS.2005.856104>
- [3] Gavade, A.B. and Rajpurohit, V.S. (2019) Systematic Analysis of Satellite Image-Based Land Cover Classification Techniques: Literature Review and Challenges. *International Journal of Computers and Applications*, **43**, 514-523. <https://doi.org/10.1080/1206212X.2019.1573946>
- [4] Talukdar, S., Singha, P., Mahato, S., Shahfahad Pal, S., Liou, Y-A. and Rahman, A. (2020) Land-Use Land-Cover Classification by Machine Learning Classifiers for Satellite Observations—A Review. *Remote Sensing*, **12**, Article No. 1135. <https://doi.org/10.3390/rs12071135>
- [5] Phiri, D., Simwanda, M., Salekin, S., Nyirenda, V.R., Murayama, Y. and Ranagalage, M. (2020) Sentinel-2 Data for Land Cover/Use Mapping: A Review. *Remote Sensing*, **12**, Article No. 2291. <https://doi.org/10.3390/rs12142291>
- [6] Pandey, P.C., Koutsias, N., Petropoulos, G.P., Srivastava, P.K. and Ben Dor, E. (2021) Land Use/Land Cover in View of Earth Observation: Data Sources, Input Dimensions, and Classifiers—A Review of the State of the Art. *Geocarto International*, **36**, 957-988. <https://doi.org/10.1080/10106049.2019.1629647>
- [7] Chughtai, A.H. and Abbasi, H. (2021) A Review on Change Detection Method and Accuracy Assessment for Land Use Land Cover. *Remote Sensing Applications. Society and Environment*, **22**, Article ID: 100482. <https://doi.org/10.1016/j.rsase.2021.100482>
- [8] Soni, P.K., Rajpal, N., Mehta, R. and Mishra, V.K. (2021) Urban Land Cover and Land Use Classification Using Multispectral Sentinel-2 Imagery. *Multimedia Tools*

- and Applications*. <https://doi.org/10.1007/s11042-021-10991-0>
- [9] Lee, J.S. and Pottier, E. (2009) Polarimetric Radar Radar Imaging. CRC Press. New York.
- [10] Nunziata, F., Migliaccio, M. and Brown, C.E. (2012) Reflection Symmetry for Polarimetric Observation of Man-Made Metallic Targets at Sea. *IEEE Journal of Oceanic Engineering*, **37**, 384-394. <https://doi.org/10.1109/JOE.2012.2198931>
- [11] Addabbo, P., Biondi, F., Clemente, C., Orlando D. and Pallotta. L. (2019) Classification of Covariance Matrix Eigenvalues in Polarimetric SAR for Environmental Monitoring Applications. *IEEE Transactions on Aerospace and Electronic Systems Magazine*, **34**, 28-43. <https://doi.org/10.1109/MAES.2019.2905924>
- [12] Pallotta, L., Clemente, C., De Maio, A. and Soraghan, J.J. (2017) Detecting Covariance Symmetries in Polarimetric SAR Images. *IEEE Transactions on Geoscience and Remote Sensing*, **55**, 80-95. <https://doi.org/10.1109/TGRS.2016.2595626>
- [13] Touzi, R., Charbonneau, F., Hawkins, R., Murnaghan, K. and Kavoun, X. (2001) Ship-sea contrast optimization when using polarimetric SARs. *International Geoscience and Remote Sensing Symposium (IGARSS '01)*, Vol. 1, Sydney, 9-13 July 2001, 426-428. <https://doi.org/10.4095/219781>
- [14] Touzi, R., Charbonneau, F., Hawkins, R. and Vachon, P. (2004) Ship Detection and Characterization Using Polarimetric SAR. *Canadian Journal of Remote Sensing*, **30**, 552-559. <https://doi.org/10.5589/m04-002>
- [15] Ringrose, R. and Harris, N. (1999) Ship Detection Using Polarimetric SAR Data. *SAR Workshop: Committee on Earth Observation Satellites (CEOS)*, Toulouse, 26-29 October 1999, 687-691.
- [16] Cameron, W.L., Youssef, N.N. and Leung, L.K. (1996) Simulated Polarimetric Signatures of Primitive Geometrical Shapes. *IEEE Transactions on Geoscience and Remote Sensing*, **34**, 793-803. <https://doi.org/10.1109/36.499784>
- [17] Kouroupis, G. and Anastassopoulos, V. (2019) Scatterer Characterization Based on the Condiagonalization of the Sinclair Backscattering Matrix. *Progress in Electromagnetics Research M*, **85**, 59-69. <https://doi.org/10.2528/PIERM19010902>
- [18] Kouroupis, G. and Anastassopoulos V. (2019) A Polarimetric CFAR ship Detector Based on the Joint Probability Function of Simulated First-Order Markov Chains. *International Journal of Remote Sensing*, **40**, 5121-5140. <https://doi.org/10.1080/01431161.2019.1579379>
- [19] Therrien, C.W. (1992) Random Processes. Prentice Hall Signal Processing Series, Prentice Hall, Hoboken.
- [20] Kouroupis, G. and Anastassopoulos, V. (2016) A Markov Chain Model Based on Cameron's CTD Ship Detection Scheme. *IEEE Imaging Systems and Techniques*, Chania, 4-6 October 2016, 100-105. <https://doi.org/10.1109/IST.2016.7738205>
- [21] Koukiou, G. and Anastassopoulos, V. (2021) Fully Polarimetric Land Cover Classification Based on Markov Chains. *Advances in Remote Sensing*, **10**, 47-65. <https://doi.org/10.4236/ars.2021.103003>
- [22] Le Hégarat-Masclé, S., Vidal-Madjar, D. and Olivier, P. (1996) Applications of Simulated Annealing to SAR Image Clustering and Classification Problems. *International Journal of Remote Sensing*, **17**, 1761-1776. <https://doi.org/10.1080/01431169608948738>
- [23] Bao, M. (1999) Classification of Multi-Temporal SAR Images and INSAR Coherence Images Using Adaptive Neighborhood Model and Simulated Annealing Approach. *Proceedings of the 20th Asia Conference on Remote Sensing*, Hong Kong

- (China), 22-25 November 1999, 811-816.
- [24] Yuan, H., Khorram, S. and Dai, X. (1999) Applications of Simulated Annealing Minimization Technique to Unsupervised Classification of Remotely Sensed Data. *IEEE 1999 International Geoscience and Remote Sensing Symposium*, Hamburg, 28 June-2 July 1999, 134-136.
- [25] Macri Pellizzeri, T., Lombardo, P., Oliver, C.J., Sciotti, M., Meloni, M. and McConnell, I. (2003) A Comparison of Statistical Segmentation Techniques for Polarimetric SAR: Region Growing versus Simulated Annealing. *Proceedings of the Workshop on POLinSAR—Applications of SAR Polarimetry and Polarimetric Interferometry* (ESA SP-529), Frascati, 14-16 January 2003, 1-6.
- [26] Manikonda, S.V.T., Sheta, A., Katangur, A. and King, S.A. (2018) Metaheuristic Search Algorithms for Oil Spill Detection Using SAR Images. 2018 *8th International Conference on Computer Science and Information Technology (CSIT)*, Amman, 11-12 July 2018, 143-149. <https://doi.org/10.1109/CSIT.2018.8486150>
- [27] Wang, L., Li, N., Zhang, Xn, Wei, T., Chen, Y.F. and Zha, J.F. (2018) Full Parameters Inversion Model for Mining Subsidence Prediction Using Simulated Annealing Based on Single Line of Sight D-InSAR. *Environmental Earth Sciences*, **77**, Article No. 161. <https://doi.org/10.1007/s12665-018-7355-0>
- [28] Strzelczyk, S.P., Strzelczyk, J., Szostek, K., Dwornik, M., Lesniak, A., Bala, J. and Franczyk, A. (2022) Information Extraction from Satellite-Based Polarimetric SAR Data Using Simulated Annealing and SIRT Methods and GPU Processing. *Energies*, **15**, Article No. 72. <https://doi.org/10.3390/en15010072>
- [29] Ertunç, E., Uyan, M. and Tongur, V. (2020) Land Reallocation Model with Simulated Annealing Algorithm. *Survey Review*, **53**, 383-389. <https://doi.org/10.1080/00396265.2020.1780406>
- [30] Sarker, S., Veremyev, A., Boginski, V. and Singh, A. (2019) Critical Nodes in River Networks. *Scientific Reports*, **9**, Article No. 11178. <https://doi.org/10.1038/s41598-019-47292-4> <https://www.nature.com/articles/s41598-019-47292-4>.
- [31] Sarker, S. (2021) Investigating Topologic and Geometric Properties of Synthetic and Natural River Networks under Changing Climate. University of Central Florida, Orlando.
- [32] Sarker, S., Veremyev, A., Boginski, V. and Singh, A. (2019) Spectral Properties of River Networks. *AGU Fall Meeting Abstracts* 2019, San Francisco, 9-13 December 2019, EP51C-2107.
- [33] Sarker, S. and Singh, A. (2017) On the Topologic Properties of River Networks. *AGU Fall Meeting Abstracts* 2017, NASA/ADS, December 2017, IN33B-0128.
- [34] Sarker, S. (2022) Essence of MIKE 21C (FDM Numerical Scheme): Application on the River Morphology of Bangladesh. *Open Journal of Modeling and Simulation*, **10**, 88-117. <https://doi.org/10.4236/ojmsi.2022.102006>
- [35] SNAP Toolboxes, Science Toolbox Exploitation Platform (n.d.). <http://step.esa.int/main/toolboxes/snap/>
- [36] Cameron, W.L. and Rais, H. (2006) Conservative Polarimetric Scatterers and Their Role in Incorrect Extensions of the Cameron Decomposition. *IEEE Transactions on Geoscience and Remote Sensing*, **44**, 3506-3516. <https://doi.org/10.1109/TGRS.2006.879115>
- [37] Maxar Technologies Ltd. (2018) RADARSAT-2 Product Description. RN-SP-52-1238 Issue 1/14.